THE JOURNAL OF PHYSICAL CHEMISTRY C
A JOURNAL OF THE AMERICAN CHEMICAL SOCIETY

pubs.acs.org/JPCC
Article

Vaterite Dissolution: Mechanism and Kinetics

Morgan P. Milner, Minjun Yang, and Richard G. Compton*

Cite This: *J. Phys. Chem. C* 2024, 128, 10388−10396
Read Online

ACCESS | Metrics & More | Article Recommendations | Supporting Information

ABSTRACT: The dissolution of porous spherulitic, vaterite particles in aqueous solution is investigated via microscopic monitoring of their size as a function of time. The latter is shown to provide a clear, generic distinction between dissolution controlled either by the rate of a surface-controlled reaction or via dissolution under conditions where the concentration of calcium and carbonate ions is pinned locally by the solubility product of vaterite followed by diffusion away from the dissolving interface into the bulk solution. Dissolution under "thermodynamic control" is shown to be the case for vaterite particles, allowing a value of the solubility product to be determined in the light of the known solution phase equilibria, including the ion pairs $CaCO_3$, $CaOH^+$, and $CaHCO_3^+$.

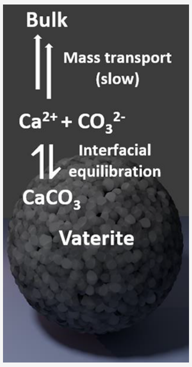

INTRODUCTION

Calcium carbonate plays a pivotal role in various natural biological and geological systems, with increasing attention given to its role in these systems arising from ecological and environmental considerations.[1] Notably, studying the involvement of calcium carbonate in the carbon cycle can offer valuable insights into atmospheric CO_2 levels.[2] In a biological context, certain marine phytoplankton have evolved to grow calcium carbonate shells which are durable and protective, with rising CO_2 levels and lower pH levels in seawater demonstrated to affect the shell growth of various phytoplankton differently.[3−5]

Crystalline calcium carbonate has three polymorphs: hexagonal vaterite, orthorhombic aragonite, and rhombohedral calcite. These have increasing thermodynamic stability and hence different solubility, with reported solubility products, K_{sp}, of 3.6×10^{-9} (calcite), 5.1×10^{-9} (aragonite), and 1.4×10^{-8} (vaterite) at 291 K, defined in terms of activities (with M as the standard state).[6] The value for vaterite is discussed later in this paper. While calcite is the most prevalent in nature due to its thermodynamic stability, all three occur, notably in the case of unstable forms in certain mollusc types.[7,8] Vaterite is particularly rare but, besides molluscs, has also been found in various sediments and rocks, is present in some bird eggs, and has been demonstrated to precipitate from the supra-glacial sulfur-containing conditions of a mineral spring in the Canadian High Arctic.[9−11] Despite the traditional applications of $CaCO_3$ in industries such as plastics, building materials, and cosmetics, a recent surge in controlled synthesis has expanded its applications to include biomaterials, drug delivery (notably from vaterite), environmental remediation, and energy production and storage.[12−16] Specifically, an increasing understanding of the nucleation and growth of $CaCO_3$ has allowed for synthesis conditions that can carefully control the dimensions, polymorphs, and morphology of synthetic $CaCO_3$ micronanoparticles (MNPs).[7,17,18] In combination with this, surface functionalization methods have been developed to tune properties such as surface hydrophobicity and reactivity.[19−21]

$CaCO_3$ MNPs of the vaterite polymorph have garnered particular attention, especially in the field of biomedicine and drug delivery. The controllable porous morphology of vaterite particles enables the incorporation of bioactive substances, ranging from small molecules to proteins and other macromolecules.[22,23] This can occur either through coprecipitation during synthesis or adsorption after particle synthesis.[16] Besides the proven biocompatibility of vaterite particles, their higher rates of dissolution in acidic environments have paved the way for applications in targeted drug delivery.[24] Specifically, the acidic environment of cancer cells can be exploited for the targeted release of drugs in the vicinity of such cells.[25,26]

To enable effective application in these areas, highly specific synthesis methods have been developed to carefully control vaterite particle properties and ensure high vaterite yield despite being the least thermodynamically stable polymorph of $CaCO_3$.[27] Vaterite can take various morphologies such as plates, lamellar aggregates, and microtablets based on synthesis conditions; however, spherulitic vaterite is preferred for most

Received: March 29, 2024
Revised: May 15, 2024
Accepted: June 4, 2024
Published: June 12, 2024

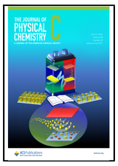

https://doi.org/10.1021/acs.jpcc.4c02074

applications, and discussion has focused on this particular form so far.[28−30] Discussion of the mechanism of growth and strategies for different syntheses is given in the Supporting Information.

The recent surge in attention to the study of $CaCO_3$ dissolution, hitherto primarily focusing on calcite, stems from its relevance in carbonate geochemistry and the acknowledgment that the ocean absorbs approximately 30% of anthropogenic CO_2.[31,32] Traditionally, methods employed to study the dissolution of micrometer-sized particles have concentrated on monitoring the release of material from a suspension over time.[33] This approach provides better than order of magnitude estimates of rate but suffers from the lack of control of mass transport, as highlighted by Sjoberg and Rickard in their pioneering work on calcite dissolution, especially under acidic conditions.[34] It also suffers from the fact that the interfacial rates, which are intrinsically local to the dissolving solid/solution boundary, are inferred from concentration measurements made in the bulk solution. The use of atomic force microscopes has facilitated the examination of the recession/growth of features, notably kinks and steps on calcite surfaces, providing mechanistic insights into particle dissolution/crystallization at the nanoscale.[35] However, this method intrinsically focuses on specific features and is not applicable for studying the global dissolution rate of micron-sized crystals as complete entities.[36] Recent work has employed an optical microscopy setup to study the dissolution reaction at a single-particle scale, providing a well-defined mass transport regime and enabling a detailed study of reaction kinetics.[36−39] In the case of vaterite, the interest in particle dissolution is potentially driven by its application in drug delivery, particularly focusing on the associated release kinetics of encapsulated substances. Classical methods for studying release kinetics often concentrate on macroscopic volumes and provide no continuous output.[40] Consequently, mechanistic insight into the dissolution of vaterite particles themselves has often been overlooked, with little work beyond simple thermodynamic solubility considerations.[6]

In this work, robust optical microscopy experiments are applied to investigate the dissolution of individual micrometer-sized spherulitic vaterite particles as single entities in aqueous solution at near neutral pH. The aim is to rigorously ascertain whether the process is controlled by the thermodynamics or surface kinetics of dissolution, as discussed in the following section, and to derive various kinetic and thermodynamic parameters.

■ THEORY

In this study, we extend the method developed by Fan et al. for investigating calcite dissolution to apply to vaterite dissolution.[38] The inverted microscopy setup, on which this is based, enables the continuous monitoring of the top-down projection area of spherical vaterite particles supported on a flat surface over time. Specifically, the previously established model, which correlates the reduction in the area of cubic calcite particles with either thermodynamic or kinetic control, has been modified for spherical vaterite particles.

When considering the dissolution of a particle resting on a planar surface, it must first be recognized that the kinetics of dissolution are based on an interplay between the rates of interfacial kinetics and mass transport of material to and from the particle surface.[36] "Kinetic control" describes the limiting case of a fast, nonrate limiting, rate of mass-transport so that the overall rate of dissolution reflects the interfacial kinetics at the particle/solution boundary. "Thermodynamic control" describes the alternative limiting case of slow, rate-determining, mass transport so that the concentration of solutes resulting from the dissolved particle and local to the particle is controlled by the solubility product of the material comprising the solid. By applying the optical microscopy method selected, the diffusional flux of material away from the particle surface can be related to the decreasing projection area and used to extract kinetic information, as outlined below.

As explained by Yang et al.,[36] to formalize the two limiting cases described above, we first consider a simplified reaction scheme for the particle surface

$$A(s) \underset{k_b}{\overset{k_f}{\rightleftharpoons}} A(aq) \xrightarrow{k_{mt}} \text{bulk} \tag{1}$$

where the rate constant k_f (mol m^{-2} s^{-1}) is for dissolution and k_b (m s^{-1}) is for the precipitation reaction, and k_{mt} (m s^{-1}) is the mass transport rate constant. By applying the steady state approximation, the overall rate of reaction, flux J, is given as

$$\text{flux } J = [A]_{ss} k_{mt} = \frac{k_f k_{mt}}{k_b + k_{mt}} \tag{2}$$

In the case of surface kinetic limitation, $k_{mt} \gg k_f$ and k_b can be applied as a condition to obtain

$$\text{flux } J \approx k_f \tag{3}$$

from eq 2. Similarly, considering thermodynamic control, we can apply the condition that $k_{mt} \ll k_f$ and k_b, so that eq 2 becomes

$$\text{flux } J \approx \frac{k_f k_{mt}}{k_b} = K_{sp} k_{mt} \tag{4}$$

Now, to consider the specific case of vaterite dissolution, we consider the reaction established at the interface

$$CaCO_3(s) \rightleftharpoons Ca^{2+}(aq) + CO_3^{2-}(aq) \tag{5}$$

Vaterite particles are closely spherical when appropriate synthesis conditions are employed, as demonstrated below by SEM imaging for our synthesized particles.[27] Hence, the number of moles of vaterite (n) in a spherical particle is given by

$$n = \frac{\rho}{M_w} \frac{4\pi r^3}{3} \tag{6}$$

where ρ (g m^{-3}) is the density of the particle, M_w = 100.1 g mol^{-1} is the molecular weight and r (m) is the radius of the sphere.[41] Differentiating eq 6 with respect to time gives an expression in terms of the total flux of Ca^{2+} and CO_3^{2-} at the particle solution interface, j:

$$j(\text{mol s}^{-1}) = \frac{dn}{dt} = -\frac{4\pi\rho r(t)^2}{M_w} \frac{dr(t)}{dt} \tag{7}$$

The minus sign accounts for the decreasing area with particle dissolution. If we normalize by the total surface area of the particle, we get

$$J(\text{mol m}^{-2}\text{ s}^{-1}) = -\frac{\rho}{R_f M_w} \frac{dr(t)}{dt} \tag{8}$$

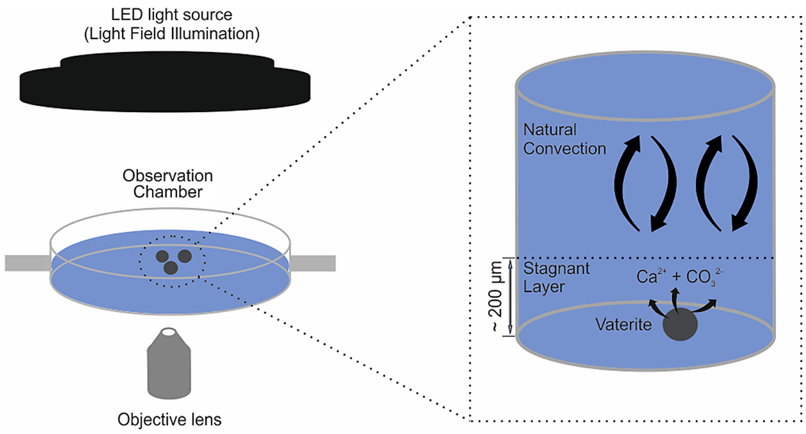

Figure 1. Schematic of the optical microscopy experimental setup.

where J (mol m^{-2} s^{-1}) now represents the flux density, and the dimensionless parameter (R_f = actual area/geometric area) is introduced as a surface roughness factor. It follows from this equation that the rate of change of particle radius with time is a constant under the constraint of kinetic control since J (mol m^{-2} s^{-1}) is expected to be a constant overall, fixed by the dissolution flux. In the experiments reported below, the size variation of the vaterite particles undergoing dissolution is tracked using an optical microscope. To determine how the projection area of particles will vary under the same constraint, we apply the chain rule to give eq 9

$$\frac{\mathrm{d}A(t)}{\mathrm{d}t} = 2\pi r(t)\frac{\mathrm{d}r(t)}{\mathrm{d}t} = -\frac{2\pi R_f M_w J}{\rho}r(t) \tag{9}$$

Note that area, A, is the projected area of the spherical particle. This demonstrates that the rate of change in the projection area is dependent on the size of the particle, which clearly decreases with time, and so is not constant, as for the case with the rate of change in particle radius.

To consider the limiting case of thermodynamic control, we recognize that the concentration of the layer adjacent to the dissolving particle is at thermodynamic equilibrium, with the fixed solute concentration determined by the solubility product. As outlined by Bobbert et al., the steady state flux from a spherical particle dissolving on a surface is given by eq 10.[42]

$$j_{ss}(\mathrm{mol\ s^{-1}}) = 4\pi Dcr\ \ln(2) \tag{10}$$

The total flux of material across the particle solution boundary is shown to be dependent on the radius of the particle r (m), the concentration of the solute at the particle−solution interface c (mol m^{-3}), and the diffusion coefficient of the solute D (m^2 s^{-1}). Normalizing by the surface area of the sphere, assuming a point contact with the surface, gives a steady state flux per unit area

$$J_{SS}(\mathrm{mol\ m^{-2}\ s^{-1}}) = \frac{\ln(2)Dc}{r} \tag{11}$$

Next, this is equated to eq 8 to produce an expression, after rearranging, for the rate of change of particle radius at the thermodynamic limit

$$\frac{\mathrm{d}r(t)}{\mathrm{d}t} = \frac{\ln(2)DcM_W}{\rho r(t)} \tag{12}$$

where R_f has been neglected since the rate is solely dependent on geometric size under thermodynamic control. Further, by applying the chain, we again generate an expression for the rate of change of the projection area of the particle with time

$$\frac{\mathrm{d}A(t)}{\mathrm{d}t} = \frac{2\pi \ln(2)DcM_W}{\rho} \tag{13}$$

From inspection of eqs 12 and 13, it is evident that the previous observation for kinetic control has now been inverted. The rate of change of the particle radius is dependent on the particles radius, while the rate of change of the projection area is independent of particle size.

This observation is key to the analysis of the experimental data reported below which were collected via the optical microscopy setup.

■ EXPERIMENTAL SECTION

Materials. Ultrapurified, deionized water with a resistivity of 18.2 MΩ cm (298 K) was used in all experiments (Milli-Q system). BioXtra grade $CaCl_2 \cdot 2H_2O$ (≥99%) was purchased from Sigma-Aldrich and reagent grade Na_2CO_3 (99.6%) from Acros Organics.

Particle Synthesis. $CaCO_3$ particles were synthesized according to the protocol outlined by Balabushevich et al., with minor adjustments.[43] The synthesis method utilizes careful control of temperature, supersaturation, stirring speed, and rate of initial mixing to ensure spherulitic vaterite formation and control size and porosity, as discussed in Section 1 of the Supporting Information.

Briefly, 3 mL of a 1 M Na_2CO_3 solution was swiftly combined with 9 mL of H_2O and 3 mL of a 1 M $CaCl_2 \cdot 2H_2O$ solution, then thoroughly mixed on a magnetic stirrer (650 rpm) for 45 s. Subsequently, the reaction mixture remained unstirred for 15 min in a water bath at 25 °C. Particles were separated through centrifugation at 2500 × g for 1 min, then resuspended in 15 mL of H_2O and centrifuged/separated again to eliminate any residual reactant salts. Lastly, the particles were suspended in 1−2 mL of methanol and air-dried at room temperature (see Supporting Information). The 15 min period prior to separation was informed by SEM images taken after 0, 15, and 90 min periods after the reaction.

Particle Characterization. X-ray diffraction patterns were obtained using a Bruker D8 Advance X-ray powder diffractometer, utilizing Cu-K$_\alpha$ radiation (λ = 1.5406 Å).

For SEM analysis, the dried $CaCO_3$ particles were spread onto carbon tape mounted on aluminum stubs. The sample was then sputtered with gold/palladium, and SEM analysis was conducted using a Zeiss Sigma 300 FEG-SEM instrument at an operating voltage of 2 kV.

To measure the surface area of the prepared crystal, N_2 adsorption−desorption analyses were conducted using a Microactive Tristar II plus instrument at 77.3 K. Before measurement, the samples underwent degassing under vacuum at room temperature for 72 h, with a low temperature chosen to minimize transformation into calcite. Surface area analysis calculations were based on the Brunauer−Emmett−Teller (BET) isotherm, as provided in Supporting Information Figures S7 and S8.[44,45]

Dissolution Experiments. The experimental methodology was based on that reported by Fan et al. and is shown schematically in Figure 1, utilizing optical microscopy to capture the top-down projection area of the dissolving calcite particle over time. For these measurements, a 20× objective (Olympus UPLXAPO 20×, Olympus Corporation, Tokyo, Japan) was employed. The illumination was provided by an LED illuminator (Aura Pro Phase Contrast Illuminator, Cairn Research, Kent, U.K.), and an ORCA-Flash 4.0 digital camera (C13440-20CU, Hamamatsu Photonics, Japan) captured the images. A custom-machined aluminum observation chamber was employed to provide an adequate volume of DI H_2O above the plane of focus to ensure the bulk ion concentration is not significantly affected by particle dissolution. The required particle concentrations are discussed below. Further in the context of dissolution on a surface, where the process is primarily driven by diffusion within a stagnant layer without convection, it is important that this layer is not constrained by the liquid surface.[46] For this reason, a depth of at least 200 μm of liquid above the particle is maintained. Experiments were carried out under ambient conditions of 20 ± 2 °C.

To maintain consistent average particle spacing, a specific mass of prepared particles was suspended in 10 mL of DI H_2O. This was promptly introduced into the observation chamber to minimize the extent of dissolution before initiating image capture. The focus under light-field illumination was optimized, and images were captured at regular time intervals based on the dissolution time scale.

Data Analysis. Images were analyzed using ImageJ freeware (Fiji). The projected area of each particle in pixels was determined using the autothresholding functions and converted to the actual projected area by multiplying the number of pixels in the image by the pixel resolution. ImageJ was also utilized for the analysis of SEM images, extracting particle and crystalline subunit size data.

PHREEQC software was used to calculate relevant equilibrium constants from $CaCO_3$ speciation when not available in the literature.

OriginPro 2023 was utilized for graph plotting and additional data analysis, including linear fitting.

RESULTS AND DISCUSSION

In the following, we first discuss the synthesis and characterization of the vaterite particles. We then report experiments on the dissolution of the vaterite quasi-spherical particles in an aqueous solution, followed by their analysis to give a clear mechanistic conclusion that the process occurs under thermodynamic control with the interfacial calcium and carbonate ions pinned by the solubility product of vaterite coupled with the diffusion of the ions away from the interface. Lastly, we discuss the inferred solubility product for vaterite in the context of prior reports.

Particle Characterization. Particle synthesis was realized by mixing solutions of $CaCl_2{\cdot}2H_2O$ and Na_2CO_3 (see the Experimental Section), followed by a 45 s stirring period and a further 15 min without stirring. The selection of the 15 min quiescent period was based on experiments, in which the 15 min period was changed to 0 and 90 min, employing SEM to investigate the impact on particle size and polymorphic outcomes. An SEM image of a single vaterite particle, as later analyzed in the dissolution study, is shown in Figure 2.

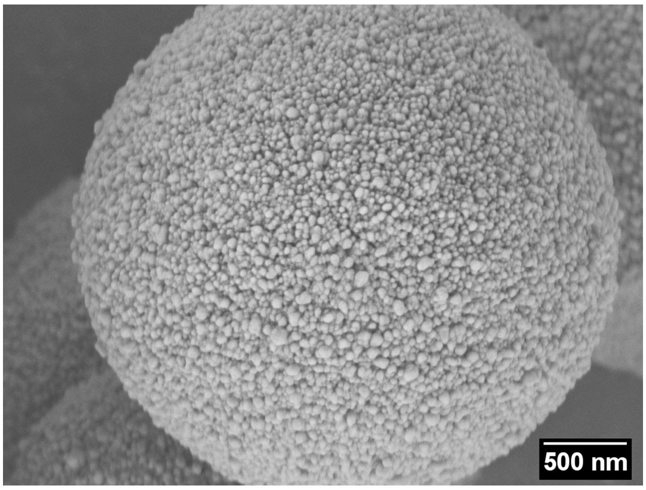

Figure 2. 30 K magnification SEM image of a single particle displaying vaterite characteristics, synthesized with a 15 min growth period.

The findings indicated that the 15 min period allows for more particle growth; while extending the duration above 15 min leads to a greater and unacceptably large degree of transformation into calcite particles. Specifically, extending this period from 0 to 15 min resulted in an increase in the average diameter of nonagglomerated spherical particles from 2.2 ± 0.5 to 2.8 ± 0.8 μm. Particles allowed to grow for 90 min, while predominantly vaterite, displayed other content that was either entirely calcite character (3%) (Figure 3a), or particles that simultaneously exhibited vaterite and calcite characteristics (10%), as shown in Figure 3b. This contrasts with 4% pure calcite particles and 2% vaterite/calcite particles in the 15 min growth synthesis. This can be understood by 15−90 min increments providing time for a significant degree of Ostwald ripening of vaterite particles to calcite through a dissolution and recrystallization process.[47,48] The images used for the analyses are given in the Supporting Information. Air drying the particles after resuspension in methanol was used to obtain dry particles for storage. This process minimizes conversion into calcite, which can occur when evaporating a water-based suspension, a method often employed.[23,43,49] This is discussed in more detail in the Supporting Information.

XRD (see SI, Figure S6) was used to confirm that particles produced under the main synthesis conditions, featuring a 15 min growth period, were a mixture of calcite and vaterite polymorphs. A surface area of 6.9 ± 0.02 $m^2\ g^{-1}$ was identified through nitrogen adsorption−desorption using the BET approach (see SI, Figures S7 and S8). The nanocrystallite particle subunits were approximately spherical, see SI for high

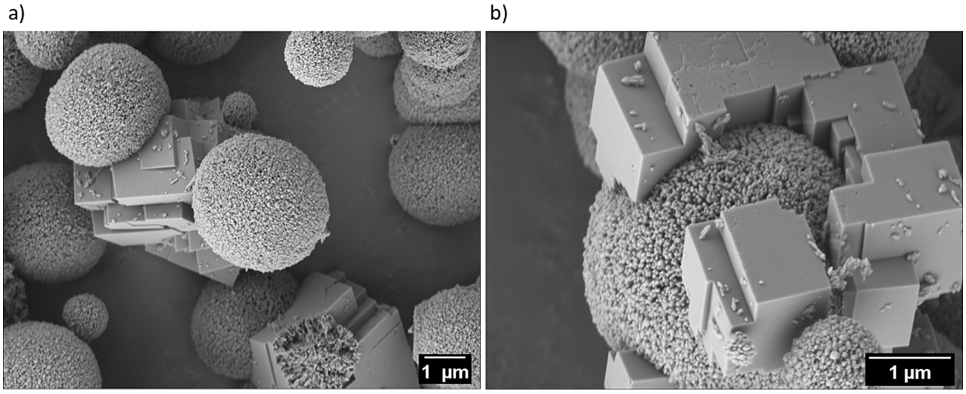

Figure 3. (a) 10 K magnification SEM image of particles synthesized with a 90 min growth period. Note the mixture of rhombohedral calcite and quasi-spherical vaterite. (b) 20 K magnification SEM image of single particle simultaneously displaying vaterite and calcite characteristics, synthesized with a 90 min growth period.

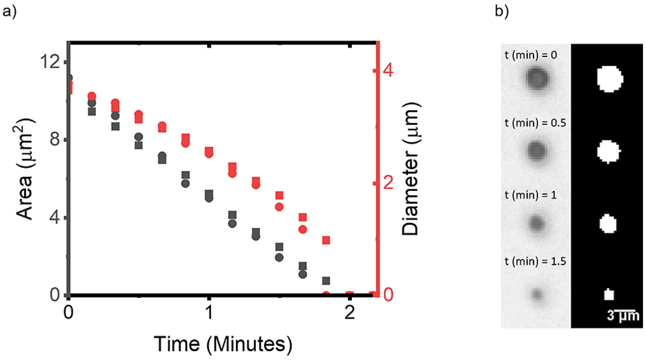

Figure 4. Measured projected area of the vaterite particles in DI water, at a concentration of 40 μg mL^{-1}, as a function of time. On the right-hand side (b), a series of optical images depict the dissolution of a vaterite particle over time. The initial particle area is 11.2 μm^2. The output after applying autothresholding are also included. On the left-hand side (a), a plot illustrates the changes in both area and diameter (assuming spherical particles throughout the entire dissolution time scale) over time. Black markers represent the area, while red markers denote the diameter. Square markers correspond to a particle with an initial area of 10.6 μm^2. Circular markers represent a different particle with an initial area of 11.2 μm^2.

magnification SEM, with an average diameter of 34 ± 2 nm. The isotherm employed for BET fitting is provided in the Supporting Information and illustrates key features of an isotherm as classified by IUPAC as a type II isotherm, indicative of macro-porous materials with pores in excess of 50 nm in width.[50]

Dissolution Experiments. The dissolution kinetics of the synthesized vaterite particles were studied using specific masses added to 10 mL of deionized water to give concentrations in the range 40 μg mL^{-1} to 450 μg mL^{-1}, and the reduction in the size of individual particles monitored over time via the inverted optical microscopy setup. This was done following the addition of the suspension to the observation chamber (see Figure 1) and allowing a small number of particles to settle on the bottom surface of the observation chamber. This allowed focus to be optimized and a set of images at regular time intervals to be recorded. For data analysis, nonagglomerated spherical particles with few, if any neighboring particles were chosen so as to avoid overlap of the diffusion fields of the different particles, which would lead to an apparent reduction of dissolution rate, and the decreasing projection area with time was extracted as outlined in the Experimental Section.

Typical data for a concentration of 40 μg mL^{-1} are shown in Figure 4, where both the diameter of the particle and the projection area are shown as a function of time. It is evident that the rate of decrease in area with time is nearly constant, in contrast with the variation of the diameter, suggesting that the dissolution is under thermodynamic control.

Typical particle diameter and projection area as a function of time plots for the maximum particle concentration studied, 450 μg mL^{-1}, are shown in Figure 5. Again, the variation of area with time shows significantly better linearity than that of the diameter, while greater variation between particles is seen as compared to the lower concentration discussed above. The plots for all concentrations studied are given in the Supporting Information, Section 4, and in all cases, the particle area, but not the diameter, changed linearly with time.

To quantify the average dissolution rate, dA/dt, over the initial part of the transient corresponding to a decrease in area to 50% of its original value, was calculated from the raw data via linear fitting. Five particles were typically studied for each concentration, and an average value over all the particles was obtained. This was repeated for different particle concentrations. The plots of area and diameter against time for all concentrations are shown in the SI. Note that data late in the transient are susceptible to more error (pixelation), and as the particle shrinks, the transition from purely thermodynamic to mixed thermodynamic/kinetic control is expected at some diameter, with both factors encouraging analysis of the earlier part of the transient.

Figure 6a shows the average rate, dA/dt plotted against concentration for the different suspensions studied. A clear trend is observed, with the gradient decreasing as the particle concentration increases. Note that as the concentration of particles changes from 40 to 450 mg mL^{-1}, the average particle separation in the solution varies approximately from 10 to 4 μm so that the imaged particles are progressively closer to other vaterite particles. The variation likely results from the overlapping of the diffusion fields of surrounding particles with those of the imaged vaterite sphere, resulting in a reduction in the apparent dissolution rate since the dissolution takes place in solutions containing already dissolved material originating from the surrounding particles. To permit consideration under conditions of infinite dilution, the data were plotted in the form of the inverse gradient against particle concentration, allowing easier extrapolation to zero concentration, as shown

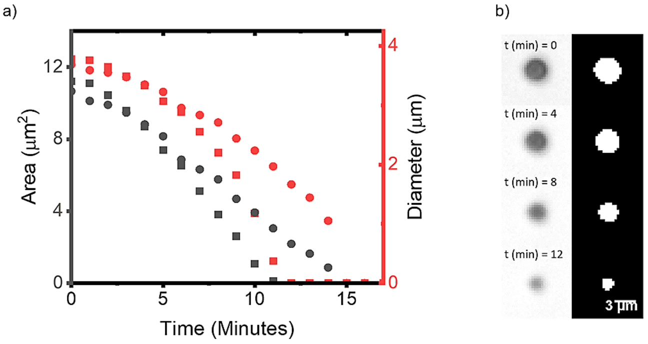

Figure 5. Measured projected area of the vaterite particles in DI water, at a concentration of 450 μg mL^{-1}, as a function of time. On the right-hand side (b), a series of optical images depict the evolution of a particle measuring 10.7 μm^2 over time. The output after applying autothresholding are also included. On the left-hand side (a), a plot illustrates the changes in both area and diameter (assuming spherical particles throughout the entire dissolution time scale) over time. Black markers represent the area, while red markers denote the diameter. Square markers correspond to a particle with an initial area of 11.2 μm^2. Circular markers represent a different particle with an initial area of 10.7 μm^2.

in Figure 6b. Fitting with a quadratic allowed the sought extrapolation, giving a rate of 1 ± 0.3 × 10^{-13} m^2 s^{-1} at infinite dilution.

The measurements of particle area versus time clearly show dissolution under thermodynamic control, where the interfacial concentration of calcite remains constant in steady-state conditions. In such cases, the rate of dissolution and the value of dA/dt are controlled by the solubility product and the rate of diffusion of the dissolved ions into the bulk solution. We therefore next consider the speciation of dissolved calcium carbonate in an aqueous solution so as to allow the inference of the solubility product of vaterite from the extrapolated rate data.

We first infer the concentration of calcium ions formed at the particle-solution interface using eq 13. The value of M_W is 100.1 g mol^{-1}, while the diffusion coefficient, D, was approximated as the average of the calcium and carbonate diffusion coefficients in aqueous solution at infinite dilution (7.25 × 10^{-10} m^2 s^{-1} at 291 K, as discussed in our previous work where the close similarity of the diffusion coefficients of the calcium and carbonate ions was noted).[38,51] The literature reports the density of vaterite as 2.6 g cm^{-3}.[52] This value, however, relates to vaterite crystals and does not account for the porosity of the synthesized spherulitic vaterite particles used here. Therefore, a density of 1.6 g cm^{-3}, as used, was related to particles synthesized using a similar procedure as adopted in this paper.[41]

Next, we assume that Ca^{2+} ions and the ion pair $\mathrm{CaCO_3}$ are fully equilibrated so that "c" in eq 13 represents the total Ca concentration defined by

$$\begin{aligned} c &= \sum [\mathrm{Ca}^{2+}]_0 \\ &= [\mathrm{Ca}^{2+}]_0 + [\mathrm{CaCO}_3^0]_0 + [\mathrm{CaHCO}_3^+]_0 + [\mathrm{CaOH}^+]_0 \end{aligned} \qquad (14)$$

where the subscript 0 implies the solution phase immediately adjacent to the dissolving solid vaterite surface.

We then consider the full set of chemical equilibria that are relevant from the chemical speciation of $\mathrm{CaCO_3}$ dissolving in water, eqs 15–21, as used in our previous model for the dissolution of calcite.[36]

$$\mathrm{CO_2(aq) + H_2O(l) \rightleftharpoons H^+(aq) + HCO_3^-(aq)} \qquad (15)$$

$$\mathrm{HCO_3^-(aq) \rightleftharpoons H^+(aq) + CO_3^{2-}(aq)} \qquad (16)$$

$$\mathrm{H_2O(l) \rightleftharpoons H^+(aq) + OH^-(aq)} \qquad (17)$$

$$\mathrm{Ca^{2+}(aq) + CO_3^{2-}(aq) \rightleftharpoons CaCO_3(s)} \qquad (18)$$

$$\mathrm{Ca^{2+}(aq) + CO_3^{2-}(aq) \rightleftharpoons {CaCO_3}^0(aq)} \qquad (19)$$

$$\mathrm{Ca^{2+}(aq) + HCO_3^-(aq) \rightleftharpoons {CaHCO_3}^+(aq)} \qquad (20)$$

$$\mathrm{Ca^{2+}(aq) + OH^-(aq) \rightleftharpoons CaOH^+(aq)} \qquad (21)$$

To solve these equations, we set conditions for conservation of mass, eq 22, and charge neutrality, as in eq 23. Note that [Carb] represents the total inorganic carbon present in the system resulting from the equilibration of water with the atmosphere.

$$\begin{aligned} &[\mathrm{Ca}^{2+}] + [\mathrm{Carb}] + [{\mathrm{CaCO}_3}^0] + [{\mathrm{CaHCO}_3}^+] + [\mathrm{CaOH}^+] \\ &\quad = [\mathrm{HCO}_3^-] + [\mathrm{CO}_3^{2-}] + [\mathrm{CO_2(aq)}] + [{\mathrm{CaHCO}_3}^+] \\ &\qquad + [{\mathrm{CaCO}_3}^0] \end{aligned} \qquad (22)$$

$$\begin{aligned} &2[\mathrm{Ca}^{2+}] + [{\mathrm{CaHCO}_3}^+] + [\mathrm{CaOH}^+] + [\mathrm{H}^+] \\ &\quad = [\mathrm{HCO}_3^-] + 2[\mathrm{CO}_3^{2-}] + [\mathrm{OH}^-] \end{aligned} \qquad (23)$$

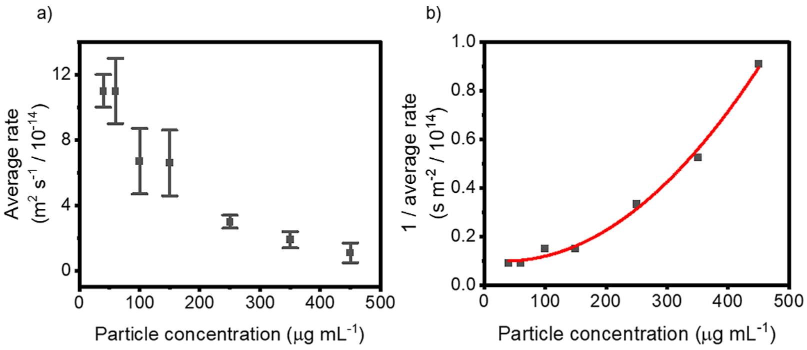

Figure 6. (a) Average rate as a function of particle concentration. The average rate was calculated from the area against time plots for five different particles at each concentration. The gradient for each plot was extracted from the region corresponding to a decrease in area to 50% of its original value. (b) Inverse average rate as a function of particle concentration. The data are fitted with a polynomial.

The equilibrium constants used for eqs 15−17 are well-documented in the literature.[53] However, those pertaining to eqs 19−21 lack sufficient reporting, necessitating their calculation using the PHREEQC software, in which activity coefficients are estimated using the Davies equation. Equations 15−23 can be solved to extract the concentrations of all free ions and ion pairs considered as a function of the solubility product (eq 18), and the value of the latter inferred such that the total calcium ion concentration (eq 14) matched the experimentally measured value of c. Note that the model contains no other adjustable parameters. The stoichiometric solubility product of vaterite, $K_{sp}{}^{0} = [Ca^{2+}][CO_3{}^{2-}]$, was thus deduced. From the inferred rate of change in the projection area with time of $1 \pm 0.3 \times 10^{-13}$ m^2 s^{-1} at infinite dilution, a $K_{sp}{}^{0}$ of $8 \pm 4 \times 10^{-8}$ at 291 K was inferred. This value relates to vaterite in the spherulitic form as characterized above and, as can be expected, is higher than the values reported by Plummer, which are inferred to relate to crystalline vaterite.[6] Note that physiological conditions will alter vaterite solubility in a drug delivery context. Specifically, based on previous studies of calcite and crystalline vaterite, increased temperature and ionic strength are expected to have contrasting effects, with temperature decreasing solubility but ionic strength increasing it.[6,36] For example, the solubility of crystalline vaterite decreases by ca. 30% if the temperature is increased from 291 to 310 K.[6] In the case of calcite, a nearly 6-fold increase in solubility was observed on going from zero ionic strength to 160 mM.[36]

■ CONCLUSIONS

We have used microscopy measurements to monitor the size of spherulitic vaterite particles as they dissolve in aqueous solution. The variation of the projected area and the particle diameter clearly shows that the particles dissolve under thermodynamic control with the concentrations of calcium and carbonate ions pinned at the dissolving interface by the solubility product of the vaterite. We demonstrated the importance of considering particle concentration, concluding that higher concentrations lead to an apparent reduction in the rate of the reaction due to the presence of enhanced solution phase ions. Therefore, data must be considered in the limit of infinite dilution of the particulate sample. From this analysis, a value for the solubility product of spherulitic vaterite was inferred and reported. The importance of accurately modeling the solution phase composition, including that of the ion pairs $CaCO_3$, $CaOH^+$, and $CaHCO_3{}^+$, is noted so as to infer a correct value of the latter. Importantly and distinct from most other methods, the loss of the solid is measured directly rather than inferred from measurements made in the bulk solution remote from the dissolving interface. The kinetic and mechanistic conclusions have important implications since porous, spherulitic vaterite is used to host pharmaceuticals, with delivery achieved *in vivo* via dissolution of the calcium carbonate host.

■ ASSOCIATED CONTENT

Supporting Information

The Supporting Information is available free of charge at https://pubs.acs.org/doi/10.1021/acs.jpcc.4c02074.

Additional particle synthesis discussion and experimental data, including particle characterization and dissolution raw data plots (PDF)

■ AUTHOR INFORMATION

Corresponding Author

Richard G. Compton − *Physical and Theoretical Chemistry Laboratory, Department of Chemistry, University of Oxford, Oxford OX1 3QZ, U.K.;* orcid.org/0000-0001-9841-5041; Email: richard.compton@chem.ox.ac.uk

Authors

Morgan P. Milner − *Physical and Theoretical Chemistry Laboratory, Department of Chemistry, University of Oxford, Oxford OX1 3QZ, U.K.*

Minjun Yang − *Centre for Sustainable Materials Processing, School of Chemistry, University of Leicester, Leicester LE1 7RH, U.K.*

Complete contact information is available at: https://pubs.acs.org/10.1021/acs.jpcc.4c02074

Author Contributions

M.M.: experiments, data analysis, and paper writing; M.Y.: conceptualization and analysis; R.G.C.: conceptualization, data interpretation, project management, and paper writing.

Notes

The authors declare no competing financial interest.

■ ACKNOWLEDGMENTS

This work was carried out with support from the University of Oxford. We thank Dr Chunhong Lei, University of Leicester, for his assistance in obtaining the powder XRD measurements.

■ REFERENCES

(1) Batchelor-McAuley, C.; Yang, M.; Rickaby, R. E. M.; Compton, R. G. Calcium Carbonate Dissolution from the Laboratory to the Ocean: Kinetics and Mechanism. Chemistry – A. *European Journal* **2022**, *28* (68), No. e202202290.

(2) Ridgwell, A.; Zeebe, R. The Role of the Global Carbonate Cycle in the Regulation and Evolution of the Earth System. *Earth Planet Sci. Lett.* **2005**, *234* (3−4), 299−315.

(3) Doney, S. C.; Fabry, V. J.; Feely, R. A.; Kleypas, J. A. Ocean Acidification: The Other CO_2 Problem. *Ann. Rev. Mar Sci.* **2009**, *1* (1), 169−192.

(4) Langer, G.; Geisen, M.; Baumann, K.; Kläs, J.; Riebesell, U.; Thoms, S.; Young, J. R. Species-specific Responses of Calcifying Algae to Changing Seawater Carbonate Chemistry. *Geochemistry, Geophysics, Geosystems* **2006**, *7* (9), No. Q09006.

(5) Yang, M.; Batchelor-McAuley, C.; Barton, S.; Rickaby, R. E. M.; Bouman, H. A.; Compton, R. G. Calcifying Coccolithophore: An Evolutionary Advantage Against Extracellular Oxidative Damage. *Small* **2023**, *19* (44), No. 2300346.

(6) Plummer, L. N.; Busenberg, E. The Solubilities of Calcite, Aragonite and Vaterite in CO2-H2O Solutions between 0 and 90°C, and an Evaluation of the Aqueous Model for the System CaCO3-CO2-H2O. *Geochim. Cosmochim. Acta* **1982**, *46* (6), 1011−1040.

(7) Niu, Y.-Q.; Liu, J.-H.; Aymonier, C.; Fermani, S.; Kralj, D.; Falini, G.; Zhou, C.-H. Calcium Carbonate: Controlled Synthesis, Surface Functionalization, and Nanostructured Materials. *Chem. Soc. Rev.* **2022**, *51* (18), 7883−7943.

(8) Mohamed, A.-M. O.; El Gamal, M.; Hameedi, S. M.; Paleologos, E. K. Mineral Carbonation. In *Sustainable Utilization of Carbon Dioxide in Waste Management*; Elsevier, 2023; pp 163−200.

(9) Friedman, G. M.; Schultz, D. J. Precipitation of Vaterite ($CaCO_3$) during Oil Field Drilling. *Mineral Mag* **1994**, *58* (392), 401−408.

(10) Jones, B. Review of Calcium Carbonate Polymorph Precipitation in Spring Systems. *Sediment Geol* **2017**, *353*, 64−75.

(11) Portugal, S. J.; Bowen, J.; Riehl, C. A Rare Mineral, Vaterite, Acts as a Shock Absorber in the Eggshell of a Communally Nesting Bird. *Ibis* **2018**, *160* (1), 173−178.

(12) Volodkin, D. CaCO3 Templated Micro-Beads and -Capsules for Bioapplications. *Adv. Colloid Interface Sci.* **2014**, *207*, 306−324.

(13) Emir, S.; Paksoy, H. New Multilayered Microencapsulated Phase Change Material with $CaCO_3$ and Ag Shells. *Energy Storage* **2021**, *3* (1), No. e214.

(14) Liu, H.; Tian, X.; Ouyang, M.; Wang, X.; Wu, D.; Wang, X. Microencapsulating N-Docosane Phase Change Material into CaCO3/Fe3O4 Composites for High-Efficient Utilization of Solar Photothermal Energy. *Renew Energy* **2021**, *179*, 47−64.

(15) Sheng, X.; Chen, S.; Zhao, Z.; Li, L.; Zou, Y.; Shi, H.; Shao, P.; Yang, L.; Wu, J.; Tan, Y.; et al. Rationally Designed Calcium Carbonate Multifunctional Trap for Contaminants Adsorption. *Science of The Total Environment* **2023**, *903*, No. 166142.

(16) Trushina, D. B.; Borodina, T. N.; Belyakov, S.; Antipina, M. N. Calcium Carbonate Vaterite Particles for Drug Delivery: Advances and Challenges. *Mater. Today Adv.* **2022**, *14*, No. 100214.

(17) Liendo, F.; Arduino, M.; Deorsola, F. A.; Bensaid, S. Factors Controlling and Influencing Polymorphism, Morphology and Size of Calcium Carbonate Synthesized through the Carbonation Route: A Review. *Powder Technol.* **2022**, *398*, No. 117050.

(18) Trushina, D. B.; Bukreeva, T. V.; Antipina, M. N. Size-Controlled Synthesis of Vaterite Calcium Carbonate by the Mixing Method: Aiming for Nanosized Particles. *Cryst. Growth Des* **2016**, *16* (3), 1311−1319.

(19) Kim, D.; Lee, J.; Lee, S.; Lim, J. Surface Modification of Calcium Carbonate Nanoparticles by Fluorosurfactant. *Colloids Surf. A Physicochem Eng. Asp* **2018**, *536*, 213−223.

(20) Yu, Y.; Zhang, J.; Wang, H.; Xin, Z. Silanized Silica-Encapsulated Calcium Carbonate@Natural Rubber Composites Prepared by One-Pot Reaction. *Polymers (Basel)* **2020**, *12* (11), 2668.

(21) Han, C.; Hu, Y.; Wang, K.; Luo, G. Preparation and In-Situ Surface Modification of CaCO3 Nanoparticles with Calcium Stearate in a Microreaction System. *Powder Technol.* **2019**, *356*, 414−422.

(22) Volodkin, D. V.; Larionova, N. I.; Sukhorukov, G. B. Protein Encapsulation via Porous CaCO $_3$ Microparticles Templating. *Biomacromolecules* **2004**, *5* (5), 1962−1972.

(23) Dunuweera, S. P.; Rajapakse, R. M. G. Synthesis of Unstable Vaterite Polymorph of Porous Calcium Carbonate Nanoparticles, Encapsulation of Anticancer Drug Cisplatin, Studying Release Kinetics for Safe, Targeted Delivery and Slow Release. *J. Nanomed. Biother. Discovery* **2017**, *7* (1), No. 1000150.

(24) Harpaz, D.; Barhom, H.; Veltman, B.; Ginzburg, P.; Eltzov, E. Biocompatibility Characterization of Vaterite with a Bacterial Whole-Cell Biosensor. *Colloids Surf. B Biointerfaces* **2023**, *222*, No. 113104.

(25) Zhu, Y.; Yang, Z.; Dong, Z.; Gong, Y.; Hao, Y.; Tian, L.; Yang, X.; Liu, Z.; Feng, L. CaCO3-Assisted Preparation of PH-Responsive Immune-Modulating Nanoparticles for Augmented Chemo-Immunotherapy. *Nanomicro Lett.* **2021**, *13* (1), 29.

(26) Kato, Y.; Ozawa, S.; Miyamoto, C.; Maehata, Y.; Suzuki, A.; Maeda, T.; Baba, Y. Acidic Extracellular Microenvironment and Cancer. *Cancer Cell Int.* **2013**, *13* (1), 89.

(27) Konopacka-Łyskawa, D. Synthesis Methods and Favorable Conditions for Spherical Vaterite Precipitation: A Review. *Crystals (Basel)* **2019**, *9* (4), 223.

(28) Li, Q.; Ding, Y.; Li, F.; Xie, B.; Qian, Y. Solvothermal Growth of Vaterite in the Presence of Ethylene Glycol, 1,2-Propanediol and Glycerin. *J. Cryst. Growth* **2002**, *236* (1−3), 357−362.

(29) Tas, A. C. Monodisperse Calcium Carbonate Microtablets Forming at 70°C in Prerefrigerated CaCl $_2$ − Gelatin−Urea Solutions. *Int. J. Appl. Ceram Technol.* **2009**, *6* (1), 53−59.

(30) Chen, J.; Xiang, L. Controllable Synthesis of Calcium Carbonate Polymorphs at Different Temperatures. *Powder Technol.* **2009**, *189* (1), 64−69.

(31) Morse, J. W.; Arvidson, R. S.; Lüttge, A. Calcium Carbonate Formation and Dissolution. *Chem. Rev.* **2007**, *107* (2), 342−381.

(32) Feely, R. A.; Sabine, C. L.; Lee, K.; Berelson, W.; Kleypas, J.; Fabry, V. J.; Millero, F. J. Impact of Anthropogenic CO $_2$ on the CaCO $_3$ System in the Oceans. *Science (1979)* **2004**, *305* (5682), 362−366.

(33) Plummer, L. N.; Wigley, T. M. L.; Parkhurst, D. L. The Kinetics of Calcite Dissolution in CO 2 -Water Systems at 5 Degrees to 60 Degrees C and 0.0 to 1.0 Atm CO 2. *Am. J. Sci.* **1978**, *278* (2), 179−216.

(34) Sjöberg, E. L.; Rickard, D. The Influence of Experimental Design on the Rate of Calcite Dissolution. *Geochim. Cosmochim. Acta* **1983**, *47* (12), 2281−2285.

(35) Arvidson, R. S.; Collier, M.; Davis, K. J.; Vinson, M. D.; Amonette, J. E.; Luttge, A. Magnesium Inhibition of Calcite Dissolution Kinetics. *Geochim. Cosmochim. Acta* **2006**, *70* (3), 583−594.

(36) Yang, M.; Tan, L.; Batchelor-McAuley, C.; Compton, R. G. The Solubility Product Controls the Rate of Calcite Dissolution in Pure Water and Seawater. *Chem. Sci.* **2024**, *15*, 2464.

(37) Morton-Collings, T.; Yang, M.; Compton, R. G. Controlling Crystallisation and Dissolution of Biogenic $CaCO_3$ *via* Dissolved Magnesium Cations. *Environmental Science: Advances* **2024**, *3*, 402.

(38) Fan, X.; Batchelor-McAuley, C.; Yang, M.; Compton, R. G. Single Calcite Particle Dissolution Kinetics: Revealing the Influence of Mass Transport. *ACS Measurement Science Au* **2022**, *2* (5), 422−429.

(39) Morton-Collings, T.; Yang, M.; Batchelor-McAuley, C.; Barton, S.; Rickaby, R. E. M.; Bouman, H. A.; Compton, R. G. A Simple Microscopy Approach Quantifies Biomineralized CO $_2$ in *Coccolithus Braarudii* − a Calcifying Marine Phytoplankton. *Environmental Science: Advances* **2023**, *2* (4), 645−651.

(40) Gusliakova, O. I.; Lengert, E. V.; Atkin, V. S.; Tuchin, V. V.; Svenskaya, Yu. I. Spectral Monitoring of Naftifine Immobilization into Submicron Vaterite Particles. *Opt. Spectrosc.* **2019**, *126* (5), 539−544.

(41) Volodkin, D. V.; Petrov, A. I.; Prevot, M.; Sukhorukov, G. B. Matrix Polyelectrolyte Microcapsules: New System for Macromolecule Encapsulation. *Langmuir* **2004**, *20* (8), 3398−3406.

(42) Bobbert, P. A.; Wind, M. M.; Vlieger, J. Diffusion to a Slowly Growing Truncated Sphere on a Substrate. *Physica A: Statistical Mechanics and its Applications* **1987**, *141* (1), 58−72.

(43) Balabushevich, N. G.; Lopez de Guerenu, A. V.; Feoktistova, N. A.; Volodkin, D. Protein Loading into Porous CaCO $_3$ Microspheres: Adsorption Equilibrium and Bioactivity Retention. *Phys. Chem. Chem. Phys.* **2015**, *17* (4), 2523−2530.

(44) Brunauer, S.; Emmett, P. H.; Teller, E. Adsorption of Gases in Multimolecular Layers. *J. Am. Chem. Soc.* **1938**, *60* (2), 309−319.

(45) Lowell, S.; Shields, J. E.; Thomas, M. A.; Thommes, M. *Surface Area Analysis from the Langmuir and BET Theories*; 2004; pp 58−81.

(46) Nernst, W. Theorie Der Reaktionsgeschwindigkeit in Heterogenen Systemen. *Zeitschrift für Physikalische Chemie* **1904**, *47U* (1), 52−55.

(47) Bots, P.; Benning, L. G.; Rodriguez-Blanco, J.-D.; Roncal-Herrero, T.; Shaw, S. Mechanistic Insights into the Crystallization of Amorphous Calcium Carbonate (ACC). *Cryst. Growth Des* **2012**, *12* (7), 3806−3814.

(48) Andreassen, J.-P.; Flaten, E. M.; Beck, R.; Lewis, A. E. Investigations of Spherulitic Growth in Industrial Crystallization. *Chem. Eng. Res. Des.* **2010**, *88* (9), 1163−1168.

(49) Pérez-Villarejo, L.; Takabait, F.; Mahtout, L.; Carrasco-Hurtado, B.; Eliche-Quesada, D.; Sánchez-Soto, P. J. Synthesis of Vaterite CaCO3 as Submicron and Nanosized Particles Using Inorganic Precursors and Sucrose in Aqueous Medium. *Ceram. Int.* **2018**, *44* (5), 5291−5296.

(50) Thommes, M.; Kaneko, K.; Neimark, A. V.; Olivier, J. P.; Rodriguez-Reinoso, F.; Rouquerol, J.; Sing, K. S. W. Physisorption of Gases, with Special Reference to the Evaluation of Surface Area and Pore Size Distribution (IUPAC Technical Report). *Pure Appl. Chem.* **2015**, *87* (9−10), 1051−1069.

(51) *CRC Handbook of Chemistry and Physics*; Haynes, W. M.; Lide, D. R.; Bruno, T. J., Eds.; CRC Press, 2016.

(52) Christy, A. G. A Review of the Structures of Vaterite: The Impossible, the Possible, and the Likely. *Cryst. Growth Des* **2017**, *17* (6), 3567−3578.

(53) Millero, F. J. The Marine Inorganic Carbon Cycle. *Chem. Rev.* **2007**, *107* (2), 308−341.